

# Elucidating the active sites and synergistic effects in water splitting on a bioinspired electrocatalyst

Thorsten O. Schmidt<sup>a,‡</sup> André Wark<sup>b,‡</sup> Richard W. Haid<sup>a</sup>, Regina M. Kluge<sup>a</sup>, Shinya Suzuki<sup>c</sup>, Kazuhide Kamiya<sup>d</sup>, Aliaksandr S. Bandarenka<sup>a,c,\*</sup> Jun Maruyama<sup>f,\*</sup> Egill Skúlason<sup>b\*</sup>

This document is the submitted manuscript version before revision of a published work that appeared in final form in T. O. Schmidt, A. Wark, R. W. Haid, R. M. Kluge, S. Suzuki, K. Kamiya, A. S. Bandarenka, J. Maruyama, E. Skúlason, Elucidating the Active Sites and Synergies in Water Splitting on Manganese Oxide Nanosheets on Graphite Support. Adv. Energy Mater. 2023, 13, 2302039. <https://doi.org/10.1002/aenm.202302039>

*a* - Physik-Department ECS, Technische Universität München, James-Frank-Straße 1, 85748 Garching, Germany

*b* - Faculty of Industrial Engineering, Mechanical Engineering and Computer Science, University of Iceland, VR-III, 107 Reykjavík, Iceland

*c* - Department of Applied Chemistry, Graduate school of engineering, The University of Tokyo, Hongo, Bunkyo-ku, Tokyo 113-8656, Japan (Present affiliation: Samsung Device

Solutions R&D Japan, Samsung Japan Corporation, 2-1-11 Senbanishi, Minoh-shi, Osaka 562-0036, Japan)

*d*- Research Center for Solar Energy Chemistry, Graduate School of Engineering Science, Osaka University, 1-3 Machikaneyama, Toyonaka, Osaka 560-8531, Japan

*e* - Catalysis Research Center TUM, Ernst-Otto-Fischer-Straße 1, 85748 Garching, Germany

*f* - Research Division of Environmental Technology, Osaka Research Institute of Industrial Science and Technology, 1-6-50 Morinomiya, Joto-ku, Osaka 536-8553, Japan

‡ - TOS and AW contributed equally to this work.

\* Corresponding authors email: E.S. [egillsk@hi.is](mailto:egillsk@hi.is), J.M. [maruyama@orist.jp](mailto:maruyama@orist.jp), A.S.B. [bandarenka@ph.tum.de](mailto:bandarenka@ph.tum.de)

## **Abstract**

It is tedious to identify active, stable, and cheap electrocatalysts. Several studies show that the most active catalysts for the oxygen evolution reaction (OER) are composite materials based on noble metals. Further research on more abundant materials is required to develop a new generation of electrocatalysts. An interesting candidate for the OER is manganese oxide ( $\text{MnO}_x$ ) which is nature's solution for the OER as a part of photosystem II. Herein, we present a  $\text{MnO}_x$ -based prototype catalyst, specifically  $\text{MnO}_2$  nanosheets deposited on a highly-oriented pyrolytic graphite (HOPG) support. We examine this catalyst's OER activity by combining classical electrochemistry, electrochemical scanning tunneling microscopy, and density functional theory calculations. We found the active sites close to the nanosheet edges and elucidated the related reaction pathway, explaining its high activity. This composite provides a more sustainable alternative to noble metal catalysts and demonstrates the potential of the metal oxide  $\text{MnO}_2$  as an energy material.

## **Keywords**

oxygen evolution reaction, manganese oxide, highly-oriented pyrolytic graphite, electrochemical scanning tunneling microscopy, density functional theory calculations, active sites, synergistic effects, noble metal-free electrocatalyst, photosystem II

## Introduction

Photosystem II (PS II) plays a key role in nature to drive the oxygen evolution reaction (OER) and can be found in plants and cyanobacteria<sup>[1,2,3]</sup>. Herein, the active site in this protein is a molecular manganese oxide cluster  $\text{Mn}_4\text{CaO}_5$ , embedded in a protein matrix, whose structure was elucidated only a decade ago<sup>[4,5]</sup>. This molecular cluster drives the photoelectrochemical water-splitting reaction at very low overpotentials (about 0.3 V at pH 5)<sup>[6]</sup>, although the underlying mechanism is still under debate. Elucidating the OER mechanism is challenging due to, among other reasons, the complicated electronic structure of the  $\text{Mn}_4\text{CaO}_5$  cluster and the complex environment of the protein matrix<sup>[7,8,9]</sup>. Nevertheless, since researchers are seeking affordable alternatives for the most efficient electrocatalytic materials, which are expensive platinum group metals, some noble-metal free and manganese dioxide ( $\text{MnO}_2$ )-based photoelectrocatalysts have been inspired by PS II<sup>[10,11,12]</sup>.

As the demand for clean and renewable fuel cells, for instance, has been increasing in the past years,  $\text{MnO}_2$ -based heterogeneous catalysts (or functionalized variants of such as it has been done for, for instance, platinum<sup>[13]</sup>) can be considered as alternative material for photoelectrocatalysis<sup>[19]</sup>. Generally, heterogeneous catalysts can better be used on a larger scale and are more persistent than homogeneous catalysts<sup>[14,15]</sup>. Moreover,  $\text{MnO}_2$  is an abundant material on earth with large deposits around the globe<sup>[16]</sup>, unlike more precious transition metal oxides such as rutile  $\text{IrO}_2$ ,  $\text{RuO}_2$ , or perovskites being utilized as the most efficient OER catalysts<sup>[17,18]</sup>. Since  $\text{MnO}_2$  has also shown to be a promising candidate as an OER catalyst<sup>[19]</sup>, far-reaching basic research is desirable to better understand the origins of these catalysts' performance. To further reduce the complexity of research in this regard, the host or substrate of the catalyst must be simplified. The ideal candidate to address this requirement is carbon which has been extensively studied in experiments and theoretically<sup>[20,21,22,23]</sup>. It is similarly abundant like  $\text{MnO}_2$ <sup>[16]</sup> and especially in its crystalline structure as highly-oriented pyrolytic graphite (HOPG). It is a popular candidate as a support material, considering its conductivity<sup>[24]</sup>, and electrochemical properties<sup>[25]</sup>, which have already been studied *in-situ*<sup>[26]</sup>, and especially under OER conditions<sup>[27,28]</sup>.

This work presents the experimental and theoretical characterization of the OER properties of the composite material  $\text{MnO}_2/\text{HOPG}$  consisting of  $\text{MnO}_2$  nanosheets ( $\text{MnO}_2\text{NS}$ ) on a HOPG support. The  $\text{MnO}_2\text{NS}$  consists of  $\text{Mn}-\text{O}_6$  octahedral units connected by shared octahedral edges forming a highly anisotropic 2D layer with a thickness of approximately 0.7 nm and a typical lateral size in the micrometer range<sup>[29,30]</sup>. Thus, the loading of  $\text{MnO}_2\text{NS}$  on HOPG forms a nearly ideal 2D model catalyst surface with broad terraces and NS step-edges with minimal height<sup>[31]</sup>. First, we present the increase in total electrochemical activity due to the presence of  $\text{MnO}_2\text{NS}$  compared to pure HOPG using linear sweep voltammetry, illustrated in a Tafel plot. Subsequently, we show the nanosheets' nature of active sites using electrochemical noise scanning tunneling microscopy (n-EC-STM), which enables an *in-situ* observation of the local activity<sup>[32]</sup>. These observations are supported and systematically explained by the most probable reaction pathways using density functional theory (DFT) calculations. Herein, the  $\text{MnO}_2\text{NS}$  were modeled as a sheet of birnessite-type  $\delta\text{-MnO}_2$ , which has been shown to have similar features to the  $\text{Mn}_4\text{CaO}_5$  in PS II<sup>[33,34]</sup>. These findings allow a fundamental understanding of the chemical process of the OER on  $\text{MnO}_2\text{NS}$ , which can be used as a foundation for further research on  $\text{MnO}_x$ -based catalyst materials.

## Results and Discussion

The catalytic activity of the MnO<sub>2</sub>NS for the OER was confirmed by higher currents for HOPG-MnO<sub>2</sub>NS compared to pure HOPG (Figure 1a and Figure S1), although the reason for the exceptionally high slope in the low current region of the semi-logarithmic plot (Tafel plot) was unknown at present but will be explained further within the DFT part of this work. The presence of the MnO<sub>2</sub>NS was confirmed by the x-ray photoelectron spectroscopy (XPS) after the electrochemical measurement (*cf.* Figure S2 in the supporting information (SI)). The low Mn/C ratio was associated with the limited number of Mn atoms within the XPS detection depth, in which the majority was C atoms of the HOPG substrate, and the Mn atoms were present only on the HOPG surface as the MnO<sub>2</sub>NS. X-ray absorption near-edge structure (XANES) (Figure S3) and the pseudo-radial structure function (RSF), being obtained by extended x-ray absorption fine structure (EXAFS) (Figure S4), further characterized the MnO<sub>2</sub>NS. The peak at around 6.56 keV in the XANES spectrum and the two peaks at around 1.47 Å and 2.49 Å of the RSF indicate that the crystal structure of the MnO<sub>2</sub>NS is a layered  $\delta$ -MnO<sub>2</sub> birnessite-type<sup>[31]</sup>. Additionally, birnessite is known to occur when MnO<sub>2</sub> is present in an electrochemical environment<sup>[34]</sup>. Consequently, it is also valid to assume that the structure of MnO<sub>2</sub>NS is birnessite-typed. Therefore, this MnO<sub>2</sub> crystal structure was utilized in our DFT calculations to model the MnO<sub>2</sub>NS.

To understand these findings and to identify the most active sites for the OER, the *in-situ* n-EC-STM technique was applied. The drawback of STMs is that it is generally unsuitable for distinguishing between different materials, and therefore, it is not straightforward to interpret the results on a composite material such as HOPG-MnO<sub>2</sub>NS. However, using specific evaluation techniques and systematically performed measurements makes it possible to identify the observed material with a high probability. First, to study the behavior of the EC-STM signal on this sample and to exclude influences by the electrolyte, a measurement in the air was performed, illustrated in Figure 1b. Here, a NS with a size of several hundred nanometers and a height of approximately 0.7 nm is measured (*cf.* line scans below and Figure S5), which agrees with other observations of MnO<sub>2</sub>NS<sup>[35,36]</sup>. The modeled height obtained from the DFT calculations is between 0.45 nm and 0.55 nm (Figures 1c and S15), which is close to the crystallographic thickness of 0.5 nm<sup>[31]</sup>. Since the measurements in Figure 1b were carried in the air, while our calculations were performed in a vacuum and at zero temperature and water and cations as spacers between the layers<sup>[34]</sup> were neglected for simplicity, both results are in reasonable agreement. Since the dimension of two overlying layers of HOPG (2 x 3.35 Å<sup>[37]</sup>) is close to the one of a single layer of MnO<sub>2</sub> (approx. 0.7 nm), it is not possible to identify the material only by the observation of the height profile in Figure 1b.

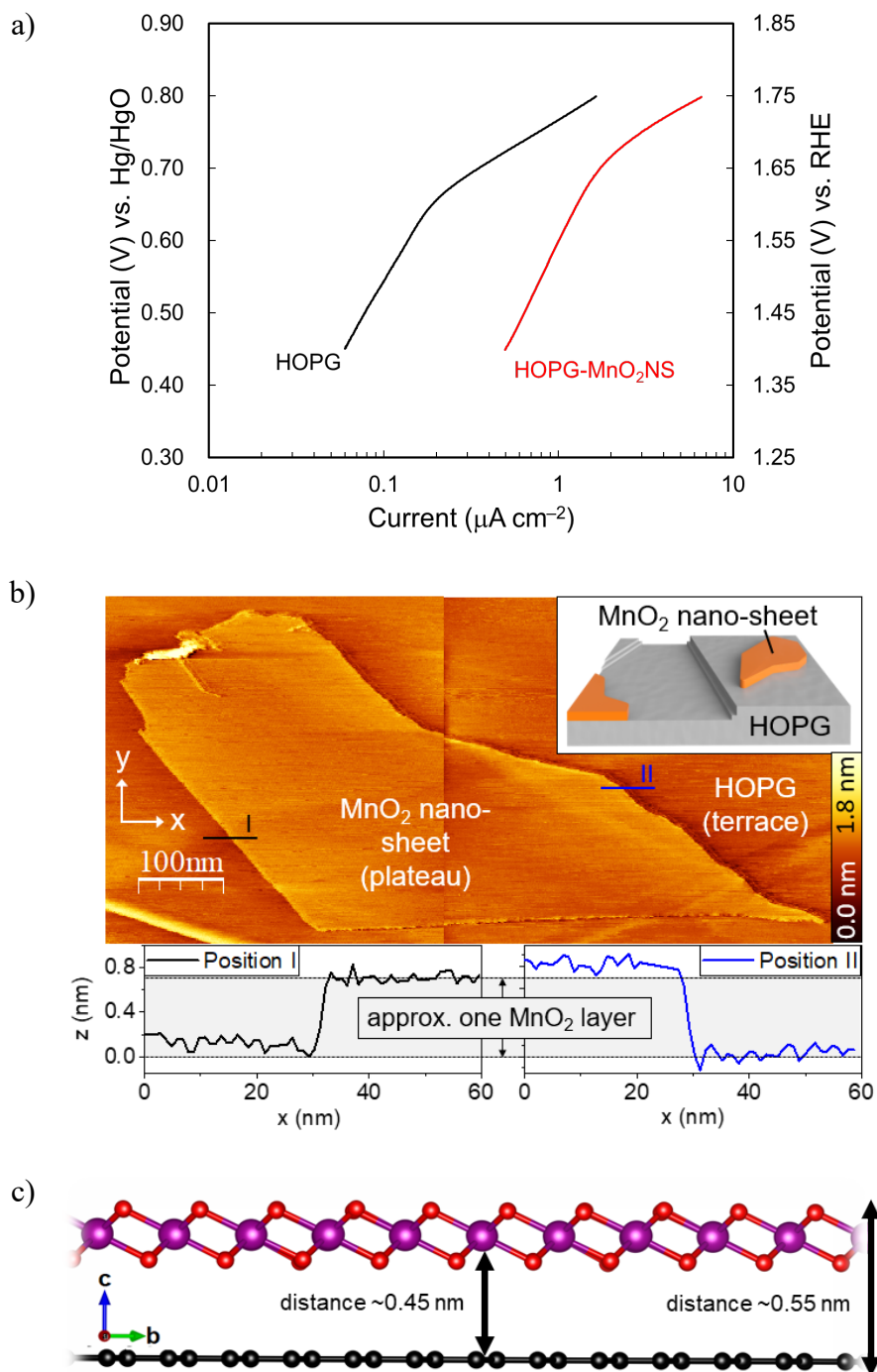


**Figure 1.** Characterization of the HOPG-MnO<sub>2</sub>NS sample. **a)** Relationships between OER current and electrode potential at HOPG and HOPG-MnO<sub>2</sub>NS in Ar-saturated 0.1 M KOH. at 25 °C. The potential scan rate was 10 mV s<sup>-1</sup>. **b)** STM measurement of a supposed MnO<sub>2</sub>NS in air and line scans of the sheet edges. Insert in the right top corner: Schematic model surface of HOPG-MnO<sub>2</sub>NS. **c)** Model of the HOPG-MnO<sub>2</sub>NS utilized in the DFT calculations. The predicted distances between the top graphene layer and the MnO<sub>2</sub>NS are shown and represented by the arrows.

A more precise determination of the materials and identification of the active sites at OER conditions is reached using the n-EC-STM technique. Like classical EC-STM, the partly insulated STM tip is engaged close to the sample surface surrounded by the electrolyte solution.

When applying a reaction potential to the sample, electrochemical processes occur at catalytically active areas and locally alter the composition of the electrolyte solution, whereby the captured tunneling current fluctuates<sup>[32,38]</sup>. This results in visible spikes in the STM signal while an increased noise level corresponds to an increased local electrochemical activity. The noise disappears as soon as the applied potential at the working electrode is set to an electrochemically “neutral” value. In this way, an identification of the nature of the active sites is possible, as shown in Figure 2. More information on this technique is available in the Methods Section and previous literature<sup>[26,27,32,39,40,41,42]</sup>.

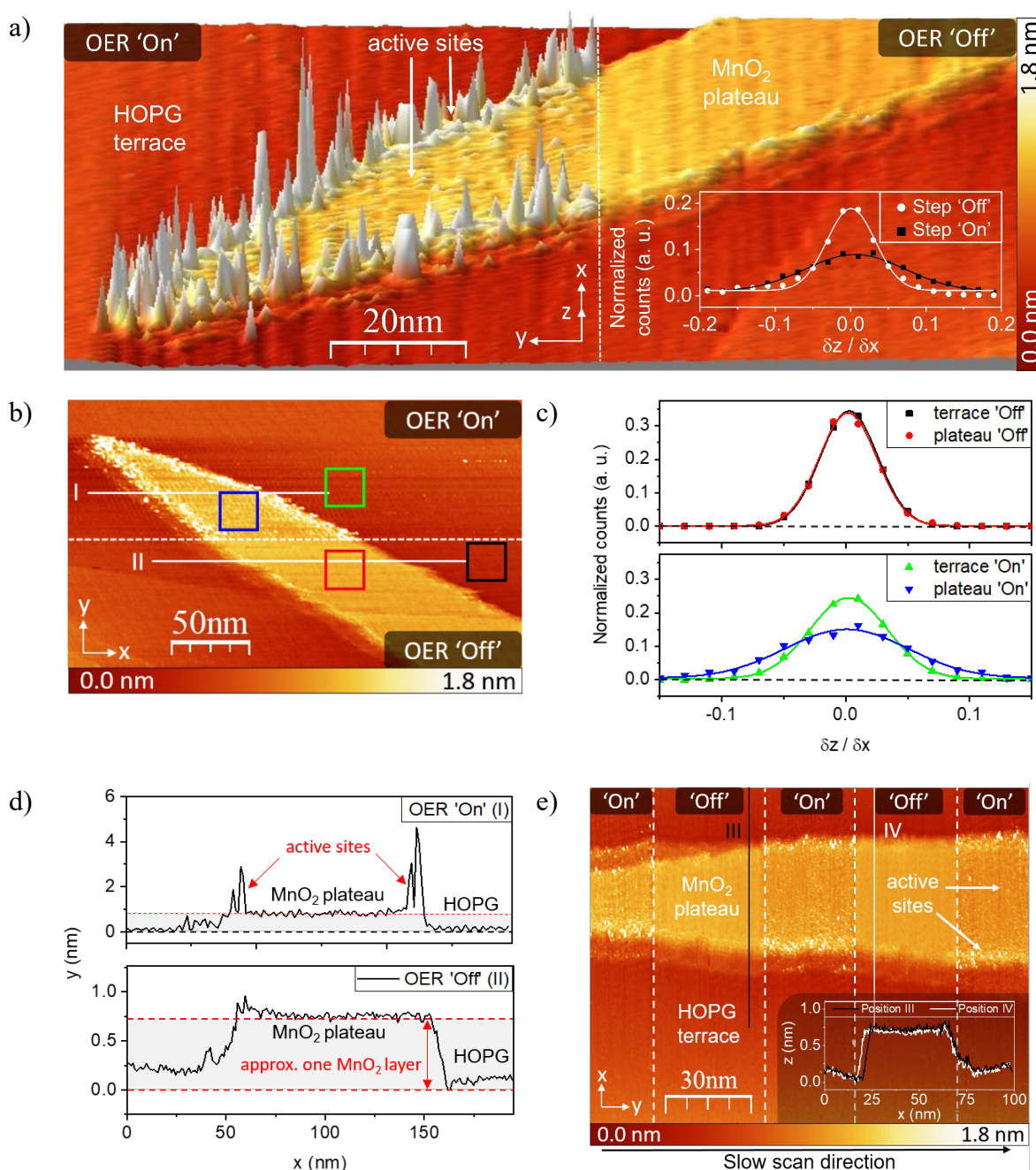


**Figure 2.** n-EC-STM measurement of an MnO<sub>2</sub>NS in 0.1 M KOH. A minor noise level increase on the MnO<sub>2</sub> sheet and exceptional noise, and thus high activity near the sheet edges is visible. **a)** Three-dimensional view of an MnO<sub>2</sub>NS (yellow area) on a HOPG support (red area). The graph in the right insert confirms a significant activity on the sheet edges for OER

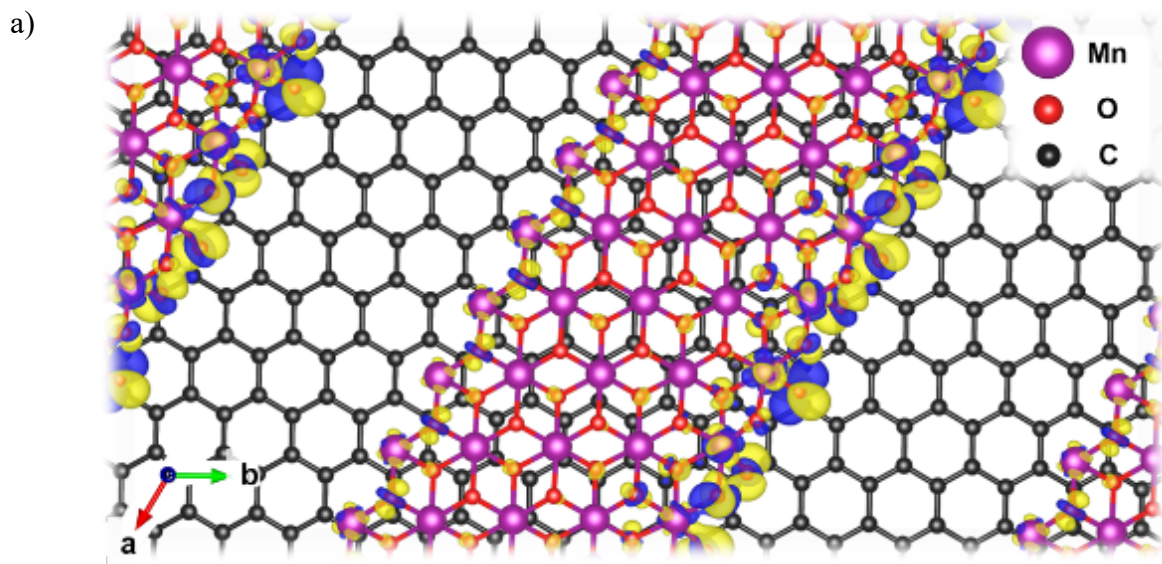
'On'. **b)** Two-dimensional top view of a) illustrating an increased noise behavior on the plateau for OER 'On' while the surrounding HOPG terrace remains rather inactive. **c)** Roughness analysis of the four areas marked in b), demonstrating the difference in the noise behavior at the plateau and the surrounding terrace. **d)** Line scans for OER 'On' (I) and 'Off' (II) highlighted as white lines in b). The active sites are found predominantly close to the sheet edges (upper graph), while the profile is almost noise-free for OER 'Off' (lower graph). **e)** Demonstration of the reproducibility of the activity behavior, including a comparison of two line scans for reaction 'Off', illustrating the absence of significant corrosion effects during the measurements.

Figure 2a shows a MnO<sub>2</sub>NS in 0.1 M KOH at a potential of 600 mV versus a Pt quasi reference electrode (mV<sub>Pt</sub>) on the left side (OER 'On') and at 0 mV<sub>Pt</sub> on the right side (OER 'Off') (*cf.* Figure S6). The significant noise behavior on the edges of the nanosheet (white spikes) for OER 'On' indicates high activity. The increased noise level disappears at OER 'Off' on the right side, confirming the origin of the noise in electrocatalytic events. The correlation becomes more obvious in the inserted graph comparing the activity on the sheet edges at OER 'Off' (white) and OER 'On' (black). Here, by counting and normalizing the derivatives of the slopes of neighboring data points, one gets information about the captured roughness which is directly related to the activity. A lower amplitude and a larger full width at half maximum (FWHM) in OER 'On' than in OER 'Off' correspond to a higher distribution of derivative slopes and, therefore, to a higher activity. A more detailed explanation of this evaluation technique is available in the Methods Section and in references [40] and [43]. A white square in Figure S7a highlights the position of the evaluated area. One beneficial side effect of using the n-EC-STM technique is the opportunity to use insights on the relative activity of surface structures to draw conclusions on the observed material. For comparison, Figure S8 shows an area that consists only of the support material HOPG without any MnO<sub>2</sub>. The active centers are equally distributed on steps and terraces and not dominantly on steps as observed in Figure 2. These findings on HOPG steps with similar experimental conditions indicate once more the correct differentiation of the materials in Figure 2a. Note that the observed noise on HOPG became visible by increased gain settings (see Table S1) and is in good agreement with the findings of a previous study<sup>[27]</sup>. Another interesting result is that under reaction conditions, the surface on top of the NS (plateau) also shows a slight activity while the surrounding HOPG is largely inactive (*cf.* Figure 2a and b), which is confirmed and explained below by our DFT calculations. By comparing the normalized number of different slopes on top of the plateau and on the surrounding terrace for OER 'On' and 'Off', a miscellaneous noise behavior is observed. While the roughness on the plateau and on the terrace is very similar for OER 'Off' (*cf.* upper graph in Figure 2c), it is significantly more pronounced on top of the plateau in contrast to the terrace for OER 'On' (*cf.* lower graph). It is likely that this difference in the noise behavior for OER 'On' results from a difference in the materials, which once more indicates MnO<sub>2</sub> as the NS material and HOPG as the subjacent layer.

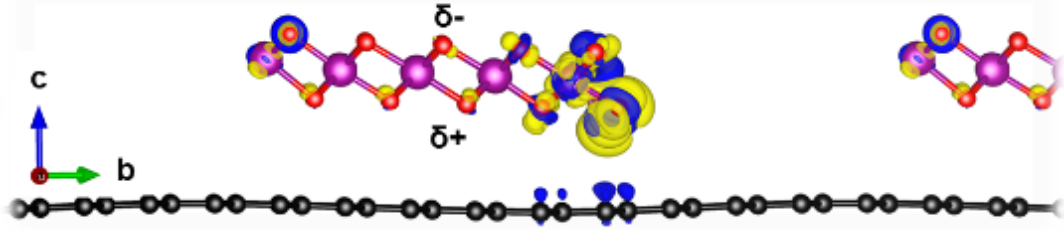
Further, Figure 2d provides a side view of the activity in representative line scans for OER 'On' (upper graph) and OER 'Off' (lower graph) with respect to the sheet height. In Figure 2e, starting on the left side of the image for OER 'On', the potential was switched 'Off' and 'On' multiple times. Neither the noise behavior nor the morphology of the sheet changed. We observed this process as reversible and did not find any evidence of corrosion during these experiments (*cf.* Figure S9). In summary, we can experimentally identify active sites on the entire MnO<sub>2</sub>NS with its highest activity close to the sheet edges, which is in accordance with the increased activity by MnO<sub>2</sub>NS illustrated in the Tafel plot in Figure 1a. To further elucidate the origin of the enhanced activity by MnO<sub>2</sub>NS and to identify the chemical moieties causing the higher

performance at their edges (Figure 2a), we performed DFT calculations as demonstrated in the following.

Figure 3 summarizes the key results of the DFT calculations. Various model systems are constructed to model the complexity of the hybrid material. To identify the synergistic effects of the hybrid material, the system is first deconvoluted into the HOPG support and the  $\text{MnO}_2$  components separately as shown in Figures S10 to S12 and S14, respectively. Our test calculation shows that using a single graphene layer is sufficient to model the HOPG support (Figures S13 and S19). The differences in the energetic landscape are negligible (Figure S19), and the charge-density-difference plots also reveal that the charge transfer from the graphite to the  $\text{MnO}_2$  sheet only originates from one graphene layer, while the other layers do not contribute to the charge transfer (Figures S38 and S39). After these calculations on the pristine components of the hybrid material, the hybrid material itself is modeled by basically two different approaches to capture the experimental situation: One model system consists of a graphene layer which is completely covered by a  $\text{MnO}_2$  sheet (Figure S16,  $\text{MnO}_2\text{NS@G}$ ) to simulate the conditions on the  $\text{MnO}_2$  plateau on which some low OER activity was detected in the n-EC-STM experiments (Figure 2a). The second model illustrated in Figures 3a and 3b (and Figures S24 and S25) also contains a graphene and  $\text{MnO}_2$  layer, but some space ("vacuum") is made between the  $\text{MnO}_2$  sheets to model the interface region (see also the results of our tests calculations in Figures S20 to S23). Within this model, we can study the catalysis of the edges of the  $\text{MnO}_2$  nanosheet (or nanoribbon) and the graphene layer. Figures 3a and 3b and S24 show a model system with one site being oxygen-terminated and the other being Mn-terminated ( $\text{MnO}_2\text{NS-1ox@G}$ ), while Figure S25 shows a model with oxygen termination on both sites ( $\text{MnO}_2\text{NS-2ox@G}$ ). Further, Figure 3c summarizes the thermodynamics of all optimal OER pathways for each of the model systems considered in this work.



b)



c)

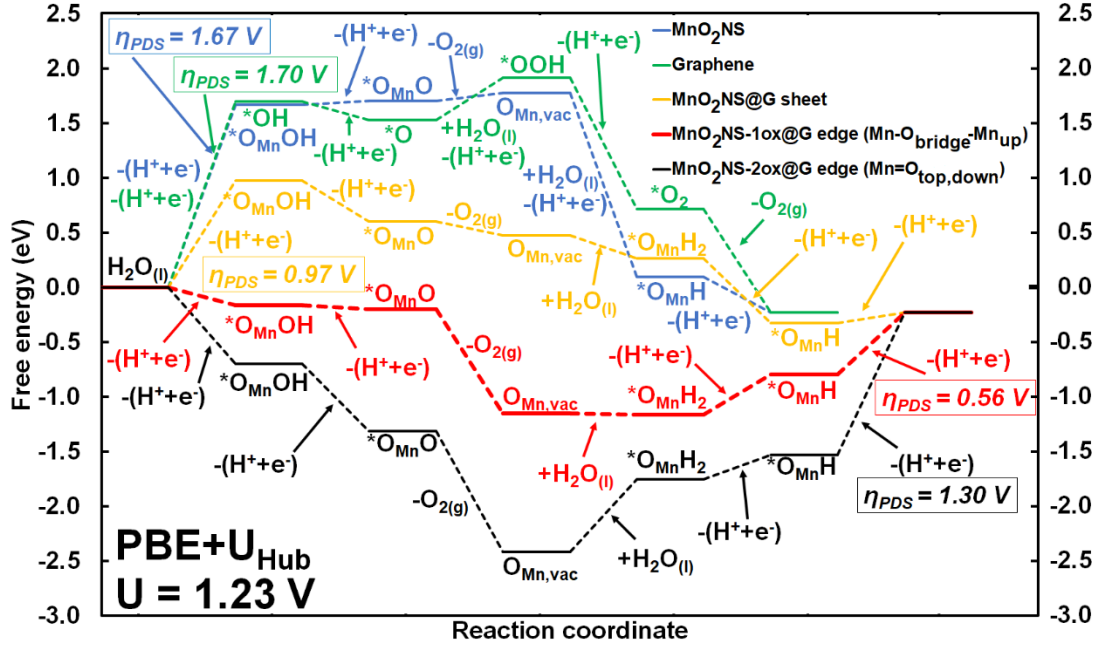


**Figure 3.** Results of the DFT calculations with **a)** showing the top and **b)** showing the side view of the MnO<sub>2</sub>NS-HOPG interface model with oxygen termination on one side and Mn termination on the other side (MnO<sub>2</sub>NS-1ox@G). Manganese, oxygen, and carbon are indicated as purple, red, and black spheres, respectively. The blue and yellow charge isosurfaces (isovalue: 0.02 e Å<sup>-3</sup>) illustrate charge depletion and charge accumulation regions, respectively. The free energy diagram in **c)** shows the calculated optimal free energy landscape of the OER of each model systems at the equilibrium potential 1.23 V vs RHE (*cf.* the catalytic cycle in Figure S18): MnO<sub>2</sub>NS (blue; shown in Figure S14); graphene (green; shown in Figure S10); ; the MnO<sub>2</sub>NS on graphene in which the MnO<sub>2</sub> fully covers the graphene (Figure S16; yellow); the MnO<sub>2</sub>NS-HOPG with one side (red, 1ox and shown in a) and b) and Figure S24) and both sides (black, 2ox, shown in Figure S25) being oxygen terminated. The first proton-electron transfer step of the OER on a MnO<sub>2</sub>NS sheet, graphene, and MnO<sub>2</sub>NS@G sheet are potential-determining on all these model systems. However, the first proton-electron transfer step on the edge site at the MnO<sub>2</sub>-graphene interface is downhill in free energy and will therefore result in small currents and low overpotentials in the experiments, as shown in Figures 1a and 2. However, the potential-determining steps of the hybrid-edge models are the last proton-electron transfer steps to complete the catalytic cycle.

The terminal oxygen atoms bound to manganese could therefore explain the detected OER activity in the experimental measurements.

Figures 3a and b reveal that a charge transfer occurs from the support material to the MnO<sub>2</sub> sheet. The same is found for other model systems like when a full sheet of MnO<sub>2</sub> completely covers the graphene support (MnO<sub>2</sub>NS@G sheet) for which Bader analysis reveals that about 0.02 e<sup>-</sup> per carbon atom are transferred to the MnO<sub>2</sub> sheet (*cf.* the charge density difference plot in Figure S38). For the supercell we use as a model system (50 carbon atoms), this corresponds to a total of 0.81 e<sup>-</sup> being transferred to the MnO<sub>2</sub> sheet. This finding is in agreement with intuition as the oxygen in the MnO<sub>2</sub> sheet is more electronegative than the carbon in the graphene support. The carbons are, therefore, more likely to be positively charged in the presence of more electronegative oxygen moieties. It is also evident from the charge-density-difference plots in Figure 3a and b that much charge density is rearranged due to the presence of the support. The charge is depleted from some Mn-O bonds and accumulates at the oxygen atoms at the edge of the nanosheet, enhancing the OER activity of hybrid material (Figure 3c). Furthermore, most charge transfer occurs from the support material to the MnO<sub>2</sub>NS around its edges (Figure 3a and b). The charge is therefore stored inside the terminal Mn-O bonds, increasing their activity even more (Figure 3c).

To justify the prediction being made by the charge-density-difference plots, the OER was modeled at various locations of the hybrid material. Basically, probing the material, like in an STM experiment, is done here by carrying out calculations in which the energetic landscape of various OER pathways at different locations or in different model systems was explored. The thermodynamics of the OER pathways at these locations in the material are summarized in Figure 3c. To identify synergistic effects within the hybrid material, the OER pathways are modeled on a pristine graphene and MnO<sub>2</sub> sheet, shown as the green and blue pathways, respectively. It is clear from these two pathways that the OER is unlikely to happen at these locations in the system, which is in agreement with the experimental observations (Figure 1a and 2a). The first proton-electron transfer step of the considered OER pathway has to surpass a high thermodynamic barrier in both cases (about 1.7 eV at U=1.23 V), where that step is also potential-determining for both systems. The given picture of the activity from the calculations agrees with the result in Figure 2a, in which it is evident that the HOPG shows negligible activity compared to other areas in the hybrid material. More activity, however, is seen on the terraces of MnO<sub>2</sub> by the n-EC-STM measurements. This situation was modeled by the model system presented in Figure S16, and the obtained OER pathway is shown in Figure 3c (yellow pathway). The first step is still potential-determining, but the overpotential is reduced by about 0.8 eV compared to the pristine components. This result indicates that the synergetic effects between the carbonaceous substrate and MnO<sub>2</sub> sheet reduce the overpotential and enhance the activity of the hybrid material. Nevertheless, the overpotential is still around 1 eV, and therefore high, and only some activity at this location would be expected here. It should be noted that the model system is only an idealized case of the experimental situation in which oxygen vacancies, for instance, could further reduce the barrier and make the hybrid material more active. However, such a situation is beyond the scope of our study and is therefore not investigated here. Nevertheless, the results already captured the qualitative trend correctly in which the hybrid material at the MnO<sub>2</sub> plateau is shown to be more active than its pristine components.

The OER at the interface region or at the edges between the carbonaceous substrate and MnO<sub>2</sub> nanosheet is also explored to complete the analysis on finding the most active sites of the overall catalyst. Here, three possible active sites can be considered: A carbon of the substrate, an oxygen which is bonded to a single manganese atom (Mn=O<sub>top</sub>), and an oxygen moiety which

bridges two manganese atoms ( $\text{Mn-O}_{\text{bridge}}\text{-Mn}$ ). The subscripts "down" and "up" indicate whether an OER intermediate is oriented in a direction to or away from the substrate, respectively, as exemplified in Figures S26 to S30 for the  $\text{Mn=O}_{\text{top,down}}$  site and Figures S31 to S35 for the  $\text{Mn-O}_{\text{bridge}}\text{-Mn}_{\text{up}}$  site. The optimal OER pathways of  $\text{MnO}_2\text{NS-1ox@G}$  and  $\text{MnO}_2\text{NS-2ox@G}$  are shown in Figure 3c in red and black, respectively, while all the others are summed up in Figures S36 and S37 in the SI. These results clearly identify the oxygen moieties at the edges of the  $\text{MnO}_2$  nanosheet as the most active sites in the hybrid system. The first proton-electron transfer step of the OER on the substrate is still thermodynamically challenging and potential-determining (Figure S36). This result was expected from the calculated OER pathway on pristine graphene (see the blue pathway in Figure 3c) and was confirmed by tests on  $\text{MnO}_2\text{NS-1ox@G}$  (see the green pathway in Figure S36). On top, the  $\text{MnO}_2\text{NS}$  are spatially more available for the reactants than HOPG as the  $\text{MnO}_2\text{NS}$  are deposited on HOPG. Consequently, the steric hindrance for the reactants to reach the edges of the  $\text{MnO}_2\text{NS}$  and to react at the interface is less than to reach HOPG. Therefore, the two oxygen moieties are shown to be the most active sites in the hybrid material (black and red pathways in Figure 3c and also Figures S36 and S37). The formations of the first OER intermediate ( $^*\text{O}_{\text{Mn}}\text{OH}$ ) at the edges require no additional potential at  $U=1.23$  V but are downhill in free energy, except for the  $\text{Mn=O}_{\text{top}}$  site in  $\text{MnO}_2\text{NS-1ox@G}$  (cf. Figure S36). It should therefore be facile to form this intermediate from a thermodynamic point of view. Significant overpotentials were found for many systems in the pathways at the edges of  $\text{MnO}_2\text{NS}$ . The OER pathway with the lowest overpotential (1.30 V at  $U = 1.23$  U) on  $\text{MnO}_2\text{NS-2ox@G}$  is shown in Figure 3c, and the step is the last deprotonation step towards the pristine hybrid system. Note that this particular step is potential-determining for all edge sites on  $\text{MnO}_2\text{NS-2ox@G}$ , but with higher overpotentials than at  $\text{Mn=O}_{\text{top,down}}$  (up to 2.0 V at  $U = 1.23$  V; Figure 3c and S37). These results raise the concern that the catalytic cycles would not be closed. Nevertheless, they can explain the activity shown in Figure 2a. Since the first step requires no extra potential to be driven, the detected current or activity is predicted to be higher than at the other investigated locations. However, it is more likely that the reaction follows at the  $\text{Mn-O}_{\text{bridge}}\text{-Mn}_{\text{up}}$  sites in the  $\text{MnO}_2\text{NS-1ox@G}$  which is shown by the red pathway in Figure 3c. Note that the  $\text{MnO}_2\text{NS}$  in the  $\text{MnO}_2\text{NS-1ox@G}$  preserve the chemical formula of  $\text{MnO}_2$ , while  $\text{MnO}_2\text{NS-2ox@G}$  is higher oxidized. The formation of the  $^*\text{O}_{\text{Mn}}\text{OH}$  intermediate at the  $\text{Mn-O}_{\text{bridge}}\text{-Mn}_{\text{up}}$  sites in  $\text{MnO}_2\text{NS-1ox@G}$  (illustrated in Figure S31) is less downhill in free energy than at most sites of the  $\text{MnO}_2\text{NS-2ox@G}$  system. However, the further pathway follows steps which require less overpotential. The overpotential of the potential-determining step, which is deprotonation of  $^*\text{O}_{\text{Mn}}\text{H}$ , is 0.56 eV (red pathway in Figure 3c). The potential-determining step at the other possible site  $\text{Mn=O}_{\text{top,down}}$  is the first deprotonation of adsorbed water and requires, however, 1.05 V overpotential at  $U = 1.23$  V (black pathway in Figure S36). Hence, the OER pathway at the  $\text{Mn-O}_{\text{bridge}}\text{-Mn}_{\text{up}}$  sites in  $\text{MnO}_2\text{NS-1ox@G}$  and this model system explain the experimental observations in Figures 1a and 2a best. Unlike the other possible reaction sites being considered in this hybrid material, this pathway's first step is thermodynamically favored at OER equilibrium potential and features a surmountable overpotential at ambient conditions. Additionally, this overpotential (0.56 V at  $U=1.23$  V) is less than for the pristine components (about 1.70 V at  $U=1.23$  V for both HOPG and  $\text{MnO}_2$ ), as it is shown in Figure 3c. These findings explain the enhanced activity (Figure 1a) and are in agreement with the n-EC-STM measurements (Figure 2a), but located the active centers even further.

Our calculations, however, do not include kinetic effects, which can determine whether the rate of an electrochemical reaction is high enough to be feasible. Particularly, the formation of peroxide intermediates ( $^*\text{OOH}$ ) has been proven to be rate-determining, which is the first step in our investigated pathways<sup>[44]</sup>. Given the system size of our models, calculations on the kinetic barriers, like by utilizing the Nudge Elastic Band<sup>[45]</sup> method, are challenging and

computationally demanding. Grand-Canonical DFT calculations on the OER on other materials could, however, reveal that also the kinetic barrier of an electrochemical reaction is reduced when the potential is applied<sup>[46,47,48,49]</sup>. Hence, and given the fact that the first step of the OER is already very downhill in energy, a kinetic barrier is assumed to be passable. The Bell-Evans-Polayni principle on the nature of transition states allows to expect a late transition state at reaction conditions and, additionally, a passable barrier. To conclude, our DFT calculations could reveal and explain not only the origin of the increased macroscopic activity but also the microscopic picture attributed to the source of activity at the edges at the interface between HOPG and the MnO<sub>2</sub>NS. Our calculations identified the oxygen atoms bound to manganese as the source of the electrochemical activity found in the experiment.

## Conclusions

In this work, we aimed to elucidate the active centers of a HOPG-MnO<sub>2</sub> hybrid material by utilizing macroscopic and microscopic methods as well as DFT calculations. After validating and characterizing the material, the Tafel plots revealed an increased catalytic performance of the hybrid material compared to pristine HOPG. To shed light on the origin of the enhanced OER activity, n-EC-STM measurements and DFT calculations were carried out. The n-EC-STM technique can assess the local activity of surface features by a distinct increase in the STM signal's noise level under reaction conditions, while the DFT calculations can further locate the active centers and the corresponding reaction pathway with atomistic resolution. The HOPG substrate remains largely inactive, as monitored by n-EC-STM images which is explained by DFT calculations by a thermodynamic barrier of 1.70 eV for the formation of the first OER intermediate. In contrast, the MnO<sub>2</sub>NS plateau is active towards the OER, however, to a lesser extent than the sites near the edges. In both cases, the formation free energy of the \*O<sub>Mn</sub>OH intermediate is decreased compared to pristine MnO<sub>2</sub>. While a significant overpotential is still calculated for the \*O<sub>Mn</sub>OH formation on the plateau, this thermodynamic barrier vanishes at the edges of the MnO<sub>2</sub>NS and a surmountable overpotential of 0.56 V at OER equilibrium potential is found there. It explains the difference in activity at both locations in the n-EC-STM experiments. Similar structural features like Mn-O<sub>bridge</sub>-Mn and Mn=O<sub>top</sub> at the edge of our hybrid material are also found in the active cluster of PS II Mn<sub>4</sub>CaO<sub>5</sub>. Therefore, our work on the simpler HOPG-MnO<sub>2</sub>NS hybrid system may provide further insights and ideas into the more complex nature of PS II. Due to the simplicity of HOPG-MnO<sub>2</sub>NS hybrid system, we could clearly assign the origin of the catalytic activity, which could help to clarify the mechanism of the OER in PS II.

## Methods

### *MnO<sub>2</sub>NS preparation*

The MnO<sub>2</sub>NS were synthesized with a method similar to those reported previously<sup>[50,51,52]</sup>. Firstly, KMnO<sub>4</sub> was heat-treated in an alumina crucible at 800 °C in the air for 10 h. The product was washed with distilled water, dried, and heat-treated again at 800 °C in the air for 20 h. An aliquot of 1 g of the obtained powder was added to 200 cm<sup>3</sup> of 1 mol dm<sup>-3</sup> HNO<sub>3</sub> and shaken for 1 day at ambient temperature. The solution was replaced with 1 mol dm<sup>-3</sup> HNO<sub>3</sub> and shaken again for 1 day. This shaking process to exchange the cations in the obtained powder was carried out for 5 days in total. After removing the solution, an aqueous solution of 200 cm<sup>3</sup> containing 2.6 g of [CH<sub>3</sub>(CH<sub>2</sub>)<sub>3</sub>]<sub>4</sub>NOH was added, shaken for 10 days at ambient temperature, and finally centrifuged at 5000 rpm to obtain the MnO<sub>2</sub>NS dispersion as the supernatant. The measurement of X-ray absorption fine structure (XAFS) was performed in air at room temperature in transmission mode using synchrotron radiation at the BL01B1 beamline of SPring-8 at the

Japan Synchrotron Radiation Research Institute. The MnO<sub>2</sub>NS dispersion was dried in vacuum and mixed with BN. The mixture was pressed to form a pellet as a sample to measure the XAFS. The RSF was obtained through Fourier transformation of the  $k^3$ -weighted EXAFS spectra using the REX2000 program (Rigaku).

#### *MnO<sub>2</sub>NS loading on HOPG*

MnO<sub>2</sub>NS were loaded on HOPG as substrates using a Langmuir-Blodgett trough (USI-3-22: trough volume, 250 cm<sup>3</sup>; trough area, 344 mm × 100 mm, USI) with a Wilhelmy plate tensiometer<sup>[53]</sup>. The trough was filled with 250 cm<sup>3</sup> of the MnO<sub>2</sub>NS dispersion diluted to 7 mg dm<sup>-3</sup>, in which typically 1 cm<sup>3</sup> of a 10% [CH<sub>3</sub>(CH<sub>2</sub>)<sub>3</sub>]<sub>4</sub>NOH solution was added. After leaving the dispersion still at 20 °C for 30 min, the surface was compressed up to the surface pressure of typically 17 mN m<sup>-1</sup> with the barrier swept at 0.5 mm s<sup>-1</sup>. Then the pressure was kept for further 30 min. The Langmuir film was transferred to the surface of the substrate, dipped vertically, and raised at 0.02 mm s<sup>-1</sup> to obtain the MnO<sub>2</sub>NS-loaded HOPG (labeled HOPG-MnO<sub>2</sub>NS).

#### *Electrochemical measurement of OER current*

The HOPG and HOPG-MnO<sub>2</sub>NS surface was masked using adhesive tape made of polytetrafluoroethylene (PTFE) with a hole of 6-mm diameter to expose the surface of 0.283 cm<sup>2</sup> and to form the working electrode. The electrochemical measurements were performed at 25 °C using an electrochemical analyzer (660B, ALS) and a three-electrode glass cell. The electrolyte was 0.1 M KOH prepared by diluting 3 M KOH (Ultrapur, Kanto Chemical) with high-purity water. The counter electrode was carbon cloth (EC-CC1-060T, ElectroChem), and the reference electrode was Hg/HgO (0.1 M KOH). The potential was repetitively scanned between 0.3 V and -0.9 V at 50 mV s<sup>-1</sup> in an Ar atmosphere until a stable voltammogram was obtained. The OER current-potential relationship was measured in an Ar atmosphere at 10 mV s<sup>-1</sup> from 0.3 V to 0.8 V. After rinsing the working electrode surface with high-purity water and drying it in air at room temperature, XPS was performed using an AXIS ULTRA DLD system (Kratos Analytical) with Al K $\alpha$  radiation (1486.6 eV).

#### *n-EC-STM*

The EC-STM setup consists of a Nanoscope III SPM Multimode (Veeco Instruments) device, a Veeco Nanoscope Universal bipotentiostat and a Nanoscope IIID controller. The MnO<sub>2</sub>/HOPG sample was clamped between a Teflon<sup>TM</sup> ring and a metal base plate, fixed by screws and served as a miniature electrochemical cell. Next to the platinum reference electrode (wire,  $\varnothing$  = 0.5 mm, 99.99%, MaTecK, Germany) and a carbon rod counter electrode (rod,  $\varnothing$  = 0.5 mm, 99.95%, Goodfellow GmbH), a mechanically cut STM-tip (wire, Pt80/Ir20,  $\varnothing$  = 0.25, 99.9+%, Goodfellow GmbH), insulated with Apiezon<sup>®</sup> wax was used. The electrolyte employed for the STM measurements at room temperature was mixed from ultrapure water (Evoqua Milli-Q<sup>®</sup>, 18.2 M $\Omega$  cm) and potassium hydroxide pellets (99.99%, Sigma Aldrich). The applied potential of 600 mV<sub>Pt</sub> for OER 'On' and of 0 mV<sub>Pt</sub> for OER 'Off' was chosen according to the significant increase of the current at approximately 550 mV<sub>Pt</sub> and the low current close to 0 mV<sub>Pt</sub> illustrated in Figure S6.

The evaluation of the images was performed by using the WSxM 5.0 Develop 9.4 software<sup>[54]</sup> and a Python script deriving the neighboring data points in the slow scan direction by using the function "numpy.gradient()" of the library NumPy and counting its relative number (*cf.* reference [40] and [43]). The normalized sums are plotted against the derivatives of the slopes with a bin size of 0.02 for 30 bins.

#### *DFT*

All spin-polarized calculations were carried out utilizing the Vienna Ab-initio Software Package (VASP; version 5.4.4)<sup>[55,56]</sup>. A dipole correction was utilized to avoid interactions between adjacent images. The functional of Perdew, Becke and Ernzerhof (PBE) was applied to carry out all simulations<sup>[57,58]</sup>. In order to account for the self-interaction error of highly localized d-electrons in manganese, the Hubbard correction with the parameter  $U_{\text{Hub}}$  was applied and set to 3.90 eV<sup>[59,60,61]</sup>. We used the projector augmented-wave (P.A.W.) method to describe the ion-core interactions<sup>[62]</sup>, choosing the following potentials: C ( $2s^2 2p^2$ , ENMAX = 400.0 eV); H ( $1s^1$ , ENMAX = 250.0 eV), O ( $2s^2 2p^4$ , ENMAX = 400.0 eV) and Mn ( $3p^6 4s^2 3d^5$ , ENMAX = 269.9 eV). The cutoff was set to 450 eV for all simulations. Convergence criteria of  $10^{-7}$  eV and  $0.01 \text{ eV } \text{\AA}^{-1}$  were used for the total energies and forces, respectively. All atoms were allowed to relax to their optimal position. Gaussian smearing with a width of 0.05 eV was applied in all cases. The following gamma point meshes were utilized for each model system<sup>[63]</sup>:  $6 \times 6 \times 1$  for graphene and graphite (two and three graphene layers) models and the hybrid material in which graphene and graphite are fully covered by a manganese oxide sheet;  $6 \times 2 \times 1$  for the interface models and  $9 \times 9 \times 1$  for a single manganese oxide sheet. All model systems with their cell constants are illustrated in Figures S10 to S12, S14, S16, S17, S24 and S25 in the SI and further described there. Furthermore, it explains the procedure to build the model systems of the hybrid material as graphene/graphite and  $\text{MnO}_2$  of the birnessite type crystallize in different structures: The pathway shown in Figure S18 was assumed for the OER on manganese oxide and the hybrid material, while the conventional mechanism is assumed for pristine graphene and graphite. To calculate the free energy of these OER pathways, the computational hydrogen electrode was utilized<sup>[64]</sup>. The free energies were obtained by correcting the DFT energies with zero-point energies (ZPEs), the entropic contribution ( $-TS$ ) and the heat capacity  $C_p dT$  which are listed in Table S2. To visualize the initial and final geometries and to calculate the charge density difference plots, the VESTA program was used<sup>[65]</sup>. Bader charges were calculated utilizing the Bader program<sup>[66]</sup>.

## Acknowledgements

TOS, RMK and ASB received funding from the European Union's Horizon 2020 research and innovation program under grant agreement HERMES No 952184. AW's work was supported by the Doctoral Fund of the University of Iceland and the Icelandic Research Fund (Grant no. 196437-051). RWH and RMK kindly acknowledges the German Research Foundation (DFG) under Germanys' excellence strategy – EXC 2089/1–390776260, the TUM IGSSE, project 11.01, and the Germany's excellence cluster "e-conversion", and under the DFG project BA 5795/6-1. JM received funding from the Network Joint Research Center for Materials and Devices (no. 20214042), a Grant-In-Aid for Scientific Research (KAKENHI; grant no. 18K04870), and the Japan Society for the Promotion of Science, and JST CREST (grant no. JPMJCR18R3). The XAFS measurements were performed with the approval of SPring-8 (Proposal No. 2019A1394). We thank Leon Haase for designing and implementing the theoretical model surface of the HOPG- $\text{MnO}_2$ NS inset in Figure 1b.

## Conflict of interest

The authors do not declare any conflict of interest.

## References

- 
- [1] Dau, H., & Haumann, M. The manganese complex of photosystem II in its reaction cycle-basic framework and possible realization at the atomic level. *Coord. Chem. Rev.*, 252, 273–295 (2008).
- [2] Zouni, A., Witt, H.-T., Kern, J., Fromme, P., Krauss, N., Saenger, W., & Orth, P. Crystal structure of photosystem II from *synechococcus elongatus* at 3.8 Å resolution. *Nature* 409, 739–743 (2001).
- [3] Menezes, P. W., Walter, C., Chakraborty, B., Hausmann, J. N., Zaharieva, I., Frick, A., Hauff, E. v., Dau, H. & Driess, M. Combination of highly efficient electrocatalytic water oxidation with selective oxygenation of organic substrates using manganese borophosphates. *Adv. Mater.* 33, 2004098 (2021).
- [4] Umena, Y., Kawakami, K., Shen, J.-R. & Kamiya, N. Crystal structure of oxygen-evolving photosystem II at a resolution of 1.9 Å, *Nature* 473, 55–61 (2011).
- [5] Shen, J. R. The structure of photosystem II and the mechanism of water oxidation in photosynthesis. *Annu. Rev. Plant Biol.* 66, 23–48 (2015).
- [6] Dau, H., Limberg, C., Reier, T., Risch, M., Roggan, S., Strasser, P. The Mechanism of Water Oxidation: From Electrolysis via Homogeneous to Biological Catalysis. *ChemCatChem* 2, 724–761 (2010).
- [7] Rossmeisl, J., Dimitrievski, K., Siegbahn, P. & Nørskov, J. K. Comparing electrochemical and biological water splitting. *J. Phys. Chem. C* 111, 18821–18823 (2007).
- [8] Zhang, B. & Sun, L. Why nature chose the Mn<sub>4</sub>CaO<sub>5</sub> cluster as water-splitting catalyst in photosystem II: A new hypothesis for the mechanism of O–O bond formation. *Dalt. Trans.* 47, 14381–14387 (2018).
- [9] Pantazis, D. A. Missing Pieces in the Puzzle of Biological Water Oxidation. *ACS Catal.* 8, 9477–9507 (2018).
- [10] Najafpour, M. M., Heidari, S., Balaghi, S. E., Hołyńska, M., Sadr, M. H., Soltani, B., Khatamian, M., Larkum, A. W. & Allakhverdiev, S. I. Proposed mechanisms for water oxidation by photosystem II and nanosized manganese oxides. *Biochim. Biophys. Acta - Bioenerg.* 1858, 156–174 (2017).
- [11] Guo, X., Liu, L., Xiao, Y., Mehmood, R., Xiao, Y., Qi, Y., & Zhang, F. Water-stable cobalt-based MOF for water oxidation in neutral aqueous solution: A case of mimicking the photosystem II. *Inorg. Chem.* 60, 1790–1796 (2021).
- [12] Najafpour, M. M., Fekete, M., Sedigh, D. J., Aro, E. M., Carpentier, R., Eaton-Rye, J. J., Nishihara, H., Shen, J.-R., Allakhverdiev, S. I. & Spiccia, L. Damage management in water-oxidizing catalysts: From photosystem II to nanosized metal oxides. *ACS Catal.* 5, 1499–1512 (2015).
- [13] Šulce, A., Backenköhler, J., Schrader, I., Delle Piane, M., Müller, C., Wark, A., Ciacci, L. C. & Kunz, S. Ligand-functionalized Pt nanoparticles as asymmetric heterogeneous catalysts:

---

molecular reaction control by ligand–reactant interactions. *Catal. Sci. Technol.* 8, 6062–6075 (2018).

[14] Pugin, B. & Blaser, H.-U. Immobilized complexes for enantioselective catalysis: when will they be used in industry?. *Top. Catal.* 53, 953-963 (2010).

[15] McMorn, P. & Hutchings, G. J. Heterogeneous enantioselective catalysts: strategies for the immobilisation of homogeneous catalysts, *Chem. Soc. Rev.* 33, 108-120 (2004).

[16] Lide, D. R. *Handbook of Chemistry and Physics, 89th Edition*, (CRC, 2008).

[17] Vojvodic, A. & Nørskov, J. K. Chemistry: optimizing perovskites for the water-splitting reaction. *Science* 334, 1355–1356 (2011).

[18] Man, I. C., Su, H. Y., Calle-Vallejo, F., Hansen, H. A., Martínez, J. I., Inoglu, N. G., Kitchin, J., Jaramillo, T. F., Nørskov, J. K. & Rossmeisl, J. Universality in oxygen evolution electrocatalysis on oxide surfaces. *ChemCatChem* 3, 1159–1165 (2011).

[19] Meng, Y., Song, W., Huang, H., Ren, Z., Chen, S. Y., & Suib, S. L. Structure - property relationship of bifunctional MnO<sub>2</sub> nanostructures: highly efficient, ultra-stable electrochemical water oxidation and oxygen reduction reaction catalysts identified in alkaline media. *J. Am. Chem. Soc.* 136, 11452-11464 (2014).

[20] Serp, P. & Figueiredo, J. L. *Carbon Materials for Catalysis* Ch. 4 (John Wiley & Sons, 2009).

[21] Sharma, S., & Pollet, B. G. Support materials for PEMFC and DMFC electrocatalysts - A review. *J. Power Sources* 208, 96-119 (2012).

[22] Gislason, P. M. & Skúlason, E. Catalytic trends of nitrogen doped carbon nanotubes for oxygen reduction reaction. *Nanoscale* 11, 18683–18690 (2019).

[23] Kirchhoff, B., Ivanov, A., Skúlason, E., Jacob, T., Fantauzzi, D., Jónsson, H. Assessment of the Accuracy of Density Functionals for Calculating Oxygen Reduction Reaction on Nitrogen-Doped Graphene. *J. Chem. Theory Comput.* 17, 6405–6415 (2021).

[24] Lechner, C., Pannier, B., Baranek, P., Forero-Martinez, N. C., & Vach, H. First-principles study of the structural, electronic, dynamic, and mechanical properties of HOPG and diamond: Influence of exchange–correlation functionals and dispersion interactions. *J. Phys. Chem. C* 120, 5083-5100 (2016).

[25] Blackman, L. C. F., & Ubbelohde, A. R. J. P Stress recrystallization of graphite. *Proc. Math. Phys. Eng. Sci.* , 266, 20-32 (1962).

[26] Kluge, R. M., Haid, R. W., Stephens, I. E. L., Calle-Vallejo, F. & Bandarenka, A. S. Monitoring active sites for hydrogen evolution reaction at model carbon surfaces. *Phys. Chem. Chem. Phys.* 23, 10051-10058 (2021).

- 
- [27] Haid, R. W., Kluge, R. M., Schmidt, T. O. & Bandarenka, A. S. In-situ detection of active sites for carbon-based bifunctional oxygen reduction and evolution catalysis. *Electrochim. Acta* 382, 138285 (2021).
- [28] Maruyama, J., Maruyama, S., Shibuya, S., & Siroma, Z. Oxygen Evolution Reaction on an Fe–N–C Catalyst Model in Water-in-Salt Electrolytes. *J. Phys. Chem. C* 127, 1855-1862 (2023).
- [29] Komaba, S., Kumagai, N. & Chiba, S. Synthesis of layered MnO<sub>2</sub> by calcination of KMnO<sub>4</sub> for rechargeable lithium battery cathode. *Electrochim. Acta* 46, 31–37 (2000).
- [30] Suzuki, S., & Miyayama, M. Preparation and electrode properties of novel redoxable nanosheets of Mn–Ni oxide with and without vacancy defects. *J. Ceram. Soc. Japan* 125, 293–298 (2017).
- [31] Fukuda, K., Nakai, I., Ebina, Y., Tanaka, M., Mori, T. & Sasaki, T. Structure analysis of exfoliated unilamellar crystallites of manganese oxide nanosheets. *J. Phys. Chem. B* 110, 17070–17075 (2006).
- [32] Pfisterer, J. H., Liang, Y., Schneider, O. & Bandarenka, A. S. Direct instrumental identification of catalytically active surface sites. *Nature* 549, 74-77 (2017).
- [33] Lu, A., Li, Y., Liu, F., Liu, Y., Ye, H., Zhuang, Z., Li, Y., Ding, H. & Wang, C. The photogeochemical cycle of Mn oxides on the Earth's surface. *Mineral Mag.* 85, 22-38 (2021).
- [34] Chernev, P., Fischer, S., Hoffmann, J., Oliver, N., Assunção, R., Yu, B., Burnap, R. L., Zaharieva, I., Nürnberg, D. J., Haumann, M. & Dau, H. Light-driven formation of manganese oxide by today's photosystem II supports evolutionarily ancient manganese-oxidizing photosynthesis. *Nat. Commun.* 11, 6110 (2020).
- [35] Kitchaev, D. A., Peng, H., Liu, Y., Sun, J., Perde, J. P. & Ceder, G. Energetics of MnO<sub>2</sub> polymorphs in density functional theory. *Phys. Rev. B* 93, 045132. (2016).
- [36] Suzuki, S. & Miyayama, M. Structural distortion in MnO<sub>2</sub> nanosheets and its suppression by cobalt substitution. *Nanomaterials* 7, 295 (2017).
- [37] Hembacher, S., Giessibl, F. J., Mannhart, J. & Quate, C. F. Revealing the hidden atom in graphite by low-temperature atomic force microscopy. *Proc. Natl. Acad. Sci.* 100, 12539-12542 (2003).
- [38] Hugelmann, M. & Schindler, W. Tunnel barrier height oscillations at the solid/liquid interface. *Surf. Sci.* 541, 1-3 (2003).
- [39] Kosmala, T., Baby, A., Lunardon, M., Perilli, D., Liu, H., Durante, C., Di Valentin, C., Agnoli, S. & Granozzi, G. Operando visualization of the hydrogen evolution reaction with atomic-scale precision at different metal–graphene interfaces. *Nat. Catal.* 4, 850 (2021).
- [40] Haid, R. W., Kluge, R. M., Liang, Y. & Bandarenka, A. S. In situ quantification of the local electrocatalytic activity via electrochemical scanning tunneling microscopy. *Small Methods* 5, 2000710 (2021).

- 
- [41] Liang, Y., Csoklich, C., McLaughlin, D., Schneider, O. & Bandarenka, A. S. Revealing active sites for hydrogen evolution at Pt and Pd atomic layers on Au surfaces. *ACS Appl. Mater. Interfaces* 11, 12476-12480 (2019).
- [42] Lunardon, M., Kosmala, T., Durante, C., Agnoli, S. & Granozzi, G. Atom-by-atom identification of catalytic active sites in operando conditions by quantitative noise detection. *Joule* 6, 617-635 (2022).
- [43] Schmidt, T. O., Ngoipala, A., Arevalo, R. L., Watzele, S. A., Lipin, R., Kluge, R. M., Hou, S., Haid, R. W., Senyshyn, A., Gubanova, E. L., Bandarenka, A. S. & Vandichel, M. Elucidation of structure-activity relations in proton electroreduction at Pd surfaces: Theoretical and experimental study. *Small* 18, 2202410 (2022).
- [44] Dickens, C. F., Kirk, C. & Nørskov, J. K. Insights into the electrochemical oxygen evolution reaction with ab initio calculations and microkinetic modeling: Beyond the limiting potential volcano. *J. Phys. Chem. C* 123, 18960-18977 (2019).
- [45] Ásgeirsson, V., Birgisson, B. O., Bjornsson, R., Becker, U., Neese, F., Riplinger, C. & Jónsson, H. Nudged elastic band method for molecular reactions using energy-weighted springs combined with eigenvector following. *J. Chem. Theory Comput.* 17, 4929–4945 (2021).
- [46] Tayyebi, E., Hoskuldsson, A. B., Wark, A., Atrak, N., Comer, B. M., Medford, A. J. & Skúlason, E. Perspectives on the competition between the electrochemical water and N<sub>2</sub> oxidation on a TiO<sub>2</sub>(110) electrode. *J. Phys. Chem. Lett.* 13, 6123–6129 (2022).
- [47] Melander, M. M., Kuisma, M. J., Christensen, T. E. K. & Honkala, K. Grand-canonical approach to density functional theory of electrocatalytic systems: Thermodynamics of solid-liquid interfaces at constant ion and electrode potentials. *J. Chem. Phys.* 150, 041706 (2019).
- [48] Melander, M. M. Grand canonical ensemble approach to electrochemical thermodynamics, kinetics, and model Hamiltonians. *Curr. Opin. Electrochem.* 29, 100749 (2021).
- [49] Van Den Bossche, M., Skúlason, E., Rose-Petruck, C. & Jónsson, H. Assessment of constant-potential implicit solvation calculations of electrochemical energy barriers for H<sub>2</sub> evolution on Pt. *J. Phys. Chem. C* 123, 4116–4124 (2019).
- [50] Kim, S. H., Kim, S. J., & Oh, S. M. Preparation of layered MnO<sub>2</sub> via thermal decomposition of KMnO<sub>4</sub> and its electrochemical characterizations. *Chem. Mat.* 11, 557-563 (1999).
- [51] Komaba, S., Kumagai, N., & Chiba, S. Synthesis of layered MnO<sub>2</sub> by calcination of KMnO<sub>4</sub> for rechargeable lithium battery cathode. *Electrochim. Acta* 46, 31-37 (2000).
- [52] Jang, H., Suzuki, S., & Miyayama, M. The role of Cu ions of the self-reassembled MnO<sub>2</sub> nanosheets for rechargeable aqueous batteries. *J. Eur. Ceram. Soc.* 34, 4297-4304 (2014).
- [53] Akatsuka, K., Haga, M. A., Ebina, Y., Osada, M., Fukuda, K., & Sasaki, T. Construction of highly ordered lamellar nanostructures through Langmuir–Blodgett deposition of

---

molecularly thin titania nanosheets tens of micrometers wide and their excellent dielectric properties. *ACS nano* 3, 1097-1106 (2009).

[54] Horcas, I., Fernández, R., Gomez-Rodriguez, J. M., Colchero, J. W. S. X., Gómez-Herrero, J. W. S. X. M., & Baro, A. M. WSXM: A software for scanning probe microscopy and a tool for nanotechnology. *Rev. Sci. Instrum.* 78, 013705 (2007).

[55] Kresse, G. & Hafner, J. Ab initio molecular dynamics for liquid metals. *Phys. Rev. B* 47, 558 (1993).

[56] Kresse, G. & Furthmüller, J. Efficiency of ab-initio total energy calculations for metals and semiconductors using a plane-wave basis set. *Comput. Mater. Sci.* 6, 15–50 (1996).

[57] Perdew, J. P., Burke, K. & Ernzerhof, M. Generalized gradient approximation made simple. *Phys. Rev. Lett.* 77, 3865 (1996).

[58] Perdew, J. P., Burke, K. & Ernzerhof, M. Erratum: Generalized gradient approximation made simple (Physical Review Letters (1996) 77 (3865)). *Phys. Rev. Lett.* 78, 1396 (1997).

[59] Dudarev, S. & Botton, G. Electron-energy-loss spectra and the structural stability of nickel oxide: An LSDA+U study. *Phys. Rev. B - Condens. Matter Mater. Phys.* 57, 1505-1509 (1998).

[60] Cococcioni, M. & De Gironcoli, S. Linear response approach to the calculation of the effective interaction parameters in the LDA+U method. *Phys. Rev. B - Condens. Matter Mater. Phys.* 71, (2005).

[61] Himmetoglu, B., Floris, A., De Gironcoli, S. & Cococcioni, M. Hubbard-corrected DFT energy functionals: The LDA+U description of correlated systems. *Int. J. Quantum Chem.* 114, 14-49 (2014).

[62] Joubert, D. From ultrasoft pseudopotentials to the projector augmented-wave method. *Phys. Rev. B - Condens. Matter Mater. Phys.* 59, 1758-1775 (1999).

[63] Monkhorst, H. J. & Pack, J. D. Special points for Brillouin-zone integrations. *Phys. Rev. B* 13, 5188-5192 (1976).

[64] Nørskov, J. K., Rossmeisl, J., Logadottir, A., Lindqvist, L. R. K. J., Kitchin, J. R., Bligaard, T., & Jonsson, H. Origin of the overpotential for oxygen reduction at a fuel-cell cathode. *J. Phys. Chem. B* 108, 17886–17892 (2004).

[65] Momma, K. & Izumi, F. VESTA 3 for three-dimensional visualization of crystal, volumetric and morphology data. *J. Appl. Crystallogr.* 44, 1272–1276 (2011).

[66] Henkelman, G., Arnaldsson, A. & Jónsson, H. A fast and robust algorithm for Bader decomposition of charge density. *Comput. Mater. Sci.* 36, 354–360 (2006).